Breakup of ^{7}Li in the field of ^{118,120}Sn nuclei and its effect on the elastic scattering channel*

N. Amangeldi[1,2] N. Burtebayev[2] G. Yergaliuly[1,3†] Maulen Nassurlla[2] B. Balabekov[1]
Abylay Tangirbergen[1,3] Awad A. Ibraheem[4] Mohamed A. Dewidar[5] Sh. Hamada[5]

[1]L.N. Gumilyov Eurasian National University, 010000 Astana, Kazakhstan
[2]Institute of Nuclear Physics, 050032 Almaty, Kazakhstan
[3]National Laboratory Astana, Nazarbayev University, Astana 010000, Kazakhstan
[4]Physics Department, King Khalid University, Abha, Saudi Arabia
[5]Faculty of Science, Tanta University, Tanta, Egypt

Abstract: The breakup of weakly-bound projectiles has been shown to significantly influence scattering processes, including elastic scattering. In this context, we revisit the angular distributions (ADs) for the elastic scattering of ^{7}Li from ^{118}Sn and ^{120}Sn targets. The study analyzes ^{7}Li + ^{118}Sn ADs over the energy range of 18.15–48 MeV and ^{7}Li + ^{120}Sn ADs from 20 to 44 MeV, utilizing various nuclear interaction models, including the São Paulo potential, CDM3Y6 potential (with and without the rearrangement term), and cluster folding model. The results indicate that the real component of the folded potentials must be scaled down by 40–65% to achieve an accurate fit to the experimental ADs, underscoring the prominent role of ^{7}Li breakup effects. Interestingly, the conventional threshold anomaly observed in reactions involving tightly bound nuclei is not present. Further analysis using the continuum discretized coupled channels (CDCC) approach provides excellent agreement with the data, reinforcing these findings.

Keywords: cluster and double folding potentials, breakup threshold anomaly, CDCC method.

DOI: 10.1088/1674-1137/ae0999 **CSTR:** 32044.14.ChinesePhysicsC.50024101

I. INTRODUCTION

The investigation of nuclear systems involving weakly-bound (WB) nuclei at energies near the Coulomb barrier (V_B) is a subject of sustained interest in nuclear physics [1, 2]. Among these WB nuclei, ^{7}Li is particularly noteworthy owing to its pronounced $\alpha + t$ structure and relatively low binding energy of approximately 2.468 MeV. Such a unique structure can significantly influence reaction mechanisms. Furthermore, investigations of nuclear reactions involving WB stable ions have revealed numerous unconventional behaviors [3].

This work focuses on understanding the scattering mechanism of ^{7}Li projectiles from ^{118,120}Sn isotopes at energies near and above the V_B. We examine the ^{7}Li + ^{118}Sn nuclear system at energies (E_{lab}) ranging from 18.15 to 48 MeV [4−6], and ^{7}Li + ^{120}Sn at E_{lab} between 20 and 44 MeV [7−9]. These systems have been the subject of extensive experimental measurements [4−12] and theoretical investigations [13−20]. Previous studies have provided valuable insights into these systems. For instance, Ref. [13] examined the scattering of ^{6,7}Li from ^{120}Sn and ^{26}Mg nuclei at E_{lab} = 44 MeV, evaluating both cross sections and analyzing powers through coupled-channel calculations. These calculations successfully reproduced the measured data when the interaction strength was significantly reduced to compensate for overestimation at the nuclear surface region. Similarly, Ref. [14] examined ^{7}Li scattering by ^{120}Sn at E_{lab} = 44 MeV within a coupled-channel framework, considering virtual projectile excitations. Both cluster folding (CF) and double-folding (DF) interactions were employed, yielding excellent agreement with experimental data for cross sections, vector analyzing power (VAP), and higher-rank tensor observables in both elastic and inelastic scattering.

The derivation of ^{7}Li+nucleus potentials has been approached through both phenomenological [16, 17] and microscopic [18, 19] methods. For instance, Cook [16] conducted simultaneous fits to multiple ^{6,7}Li datasets spanning mass numbers 24−208 to establish a global optical potential (OP) for ^{6,7}Li scattering. The analysis revealed that Woods-Saxon (WS) form factors with constant parameters could be used for all potential components except the imaginary potential depth, which de-

Received 10 August 2025; Accepted 22 September 2025; Published online 23 September 2025

* This work was carried out by the Science Committee of the Ministry of Science and Higher Education of the Republic of Kazakhstan (AP26194167)

† E-mail: yergaliuly.gani@gmail.com

creased with increasing target mass. Notably, the real potential depth was found to be identical for projectiles, resulting in a smaller volume integral for ^{7}Li. Additionally, the imaginary volume integral was smaller for ^{7}Li than for ^{6}Li, indicating weaker absorption for ^{7}Li.

In a complementary study, Y. Xu *et al.* [17] proposed a global phenomenological optical model (OM) potential for ^{7}Li projectiles, based on elastic scattering ADs and reaction cross-section (σ_R) data for target nuclei ranging from ^{27}Al to ^{208}Pb at energies below 200 MeV. This potential provided satisfactory descriptions of ^{7}Li elastic scattering across the studied systems. Microscopic approaches have also contributed significantly to our understanding. Xu and Pang [18] introduced a global potential by analyzing ADs from ^{6,7}Li elastic scattering off targets ($A \geq 40$) at $E_{\rm lab}$ = 5–40 MeV/u. The single-folding model, incorporating the *JLMB* nucleon-nucleus interaction [21, 22] provided good agreement with experimental σ_R and AD data. In a more fundamental approach, Chen *et al.* [19] developed a microscopic OP for ^{7}Li+nucleus systems without adjustable parameters. This potential was constructed by folding the microscopic OP of the cinstitutent nucleons of ^{7}Li over their density distributions, with the internal wave function described using the harmonic oscillator shell model. The resulting potential successfully predicted ADs and $\sigma_{\rm R}$ for targets ranging from A = 27 to 208 at energies below 450 MeV, demonstrating comparable performance to that of global phenomenological potentials. Basak *et al.* [20] provided additional insights through the analysis of elastic scattering cross sections and VAP for ^{6,7}Li scattered from ^{12}C, ^{26}Mg, ^{58}Ni, and ^{120}Sn nuclei. Their OM calculations employed a real folded potential based on realistic two-nucleon interactions, requiring no normalization, along with imaginary and spin-orbit potentials. This approach successfully accounted for both cross section and VAPs, including the explanation of opposite signs observed in VAP data for ^{6,7}Li + ^{58}Ni and ^{6,7}Li + ^{120}Sn systems at $E_{\rm lab}$ = 20 and 44 MeV, respectively.

This work presents a comprehensive investigation of elastic scattering cross sections for ^{7}Li projectiles on ^{118,120}Sn targets across a broad energy range. Utilizing multiple nuclear potential models and computational approaches, we systematically compare theoretical predictions with experimental data. A key focus of our analysis is the determination of the necessary normalization factors required to achieve optimal agreement with the AD data for both ^{7}Li + ^{118}Sn and ^{7}Li + ^{120}Sn systems. The rest of this paper is structured as follows: Sec. II details the theoretical framework and potential models employed in our calculations, Sec. III presents and analyzes the results, and Sec. IV summarizes our principal findings and conclusions.

II. THEORETICAL FRAMEWORK AND IMPLEMENTED POTENTIALS

The elastic scattering ADs for the systems ^{7}Li + ^{118}Sn at $E_{\rm lab}$ = 18.15–48 MeV and ^{7}Li + ^{120}Sn at $E_{\rm lab}$ = 20–44 MeV have been reanalyzed using a systematic hierarchy of theoretical approaches. We begin with microscopic methods, including the São Paulo potential (SPP) and double-folding potentials (DFPs), advance to cluster folding potential (CFP) to explicitly account for the distinctive $\alpha + t$ configuration of ^{7}Li, and ultimately employ the comprehensive continuum discretized coupled channels (CDCC) technique. This methodological progression provides complementary insights into the scattering dynamics and facilitates the identification of optimal interaction potentials that accurately reproduce the experimental ADs. The **FRESCO** code [23] was employed for the calculations, supplemented by **SFRESCO** extensions for χ^2 minimization, which facilitated the accurate extraction of optimal potential parameters to fit the data.

A. São Paulo potential

The SPP offers a microscopic description of the nuclear interaction. This approach derives the potential through DF procedures that explicitly incorporate the nucleon-nucleon interaction potential (V_{NN}) with realistic nuclear densities. The SPP formulation shares conceptual similarities with conventional DF potentials but maintains distinct advantages in its theoretical foundation. For the current analysis, the nuclear density distributions of ^{7}Li and ^{118,120}Sn were obtained from high-precision Dirac-Hartree-Bogoliubov (DHB) calculations, as tabulated by the **REGINA** code [24]. These microscopic densities provide a more rigorous basis for potential generation compared to phenomenological parameterizations. Figure 1 presents the complete set of derived SPPs for both systems across the investigated energy ranges. Within the SPP approach used here, the imaginary part of the potential is constructed to be proportional to the real part, sharing the same radial form factor, and with a separate normalization factor.

B. Double folding potentials

The ^{7}Li + ^{118,120}Sn systems were also investigated within the microscopic DF model using CDM3Y6 interactions. This analysis employed the same nuclear density distributions derived from the DHB model [24] as used in the SPP framework, ensuring consistency, while focusing specifically on the differences arising from the interaction potential. The **DFMSPH** code [25] generated the DFPs across the studied energy ranges by folding the projectile and target densities with the interaction potential (V_{NN}):

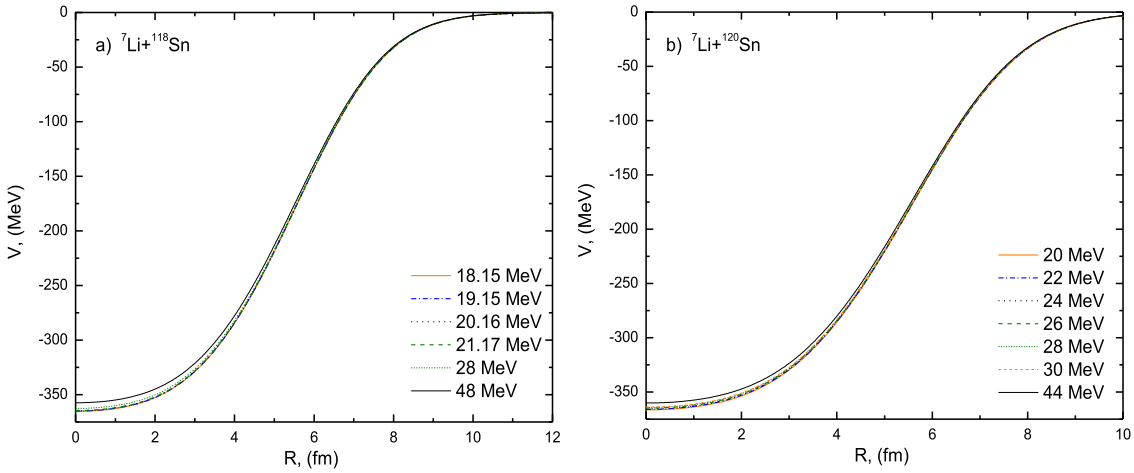

Fig. 1. (color online) SPP for a) ^{7}Li+^{118}Sn at $E_{\rm lab}$ = 18.15, 19.15, 20.16, 21.17, 28, and 48 MeV and b) ^{7}Li+^{120}Sn at $E_{\rm lab}$ = 20, 22, 24, 26, 28, 30, and 44 MeV.

$$V^{DF}(R) = \int \rho_p(r_p)\,\rho_t(r_t)\,V_{NN}(s)\,\mathrm{d}^3 r_p\,\mathrm{d}^3 r_t\,,\ s = r_t - r_p + R. \tag{1}$$

The V_{NN} (CDM3Y6 interaction) based on the M3Y-Paris potential incorporates both direct $v_{\rm D}(s)$ and exchange $v_{\rm EX}(s)$ components, which are density and energy- dependent:

$$v_{\rm D(EX)}(\rho, s) = F(\rho) g(E) v_{\rm D(EX)}(s), \tag{2}$$

where s is the separation between two interacting nucleons and ρ is the nuclear matter density. This functional dependence accounts for the nuclear medium effects on the effective interaction, assuming the form [26]

$$F(\rho) = 0.2658[1 + 3.8033\exp(-1.4099\rho) - 4.0\rho]. \tag{3}$$

The energy-dependent factor $g(E)$ is expressed as [27]

$$g(E) = 1 - 0.003(E/A) g(E) = 1 - 0.003(E/A). \tag{4}$$

To explore additional physical effects, we implemented a modified version, CDM3Y6-RT, that incorporates the rearrangement term (RT) through an additional density-dependent correction $\Delta F(\rho)$ [28]:

$$\Delta F(\rho) = 1.5\left[\exp(-0.833\rho) - 1\right]. \tag{5}$$

The rearrangement term $\Delta F(\rho)$ accounts for the energy dependence arising from the variation in the single-nucleon potential with density, representing a correction due to the reorganization of the nuclear medium during the interaction. The direct and exchange components of the effective NN interaction are scaled by the modified density-dependent function $\left[F_{\rm RT}(\rho) = \Delta F(\rho) + F(\rho)\right]$ before the folding integral is calculated. This results in a microscopically motivated, energy-dependent correction to the real part of the folded potential. The resulting CDM3Y6 and CDM3Y6-RT potential forms are displayed in Fig. 2.

C. Cluster folding potential

The cluster folding model (CFM) formalism was specifically employed to incorporate the well-established $\alpha + t$ cluster configuration of the ^{7}Li nuclei, which is particularly significant considering the modest binding energy of only 2.468 MeV. This approach constructs the effective potential through careful consideration of the individual α+target and t+target interactions, properly weighted by the cluster relative wave function $\chi_{\alpha-t}(r)$ as follows:

$$V^{CF}(R) = \int \left[V_{\alpha+^{118}{\rm Sn}\,(^{120}{\rm Sn})}\left(R - \frac{3}{7}r\right) + V_{t+^{118}{\rm Sn}(^{120}{\rm Sn})}\left(R + \frac{4}{7}r\right)\right] |\chi_{\alpha-t}(r)|^2 \mathrm{d}\,r, \tag{6}$$

$$W^{CF}(R) = \int \left[W_{\alpha+\,^{118}{\rm Sn}(^{120}{\rm Sn})}\left(R - \frac{3}{7}r\right) + W_{t+^{118}{\rm Sn}(^{120}{\rm Sn})}\left(R + \frac{4}{7}r\right)\right] |\chi_{\alpha-t}(r)|^2 \mathrm{d}\,r, \tag{7}$$

where $(V_{\alpha+\,^{118}{\rm Sn}(^{120}{\rm Sn})}, V_{t+^{118}{\rm Sn}(^{120}{\rm Sn})})$ and $(W_{\alpha+\,^{118}{\rm Sn}(^{120}{\rm Sn})}, W_{t+^{118}{\rm Sn}(^{120}{\rm Sn})})$ are the real and imaginary potentials for the α + ^{118}Sn(^{120}Sn) and t + ^{118}Sn(^{120}Sn) subsystems, respectively. These constituent potentials reproduce experimental data at energies $E_\alpha \approx 4/7E_{\rm Li}$ and $E_t \approx 3/7E_{\rm Li}$. The α+t bound state (^{7}Li ground state) is described by a $2P_{3/2}$

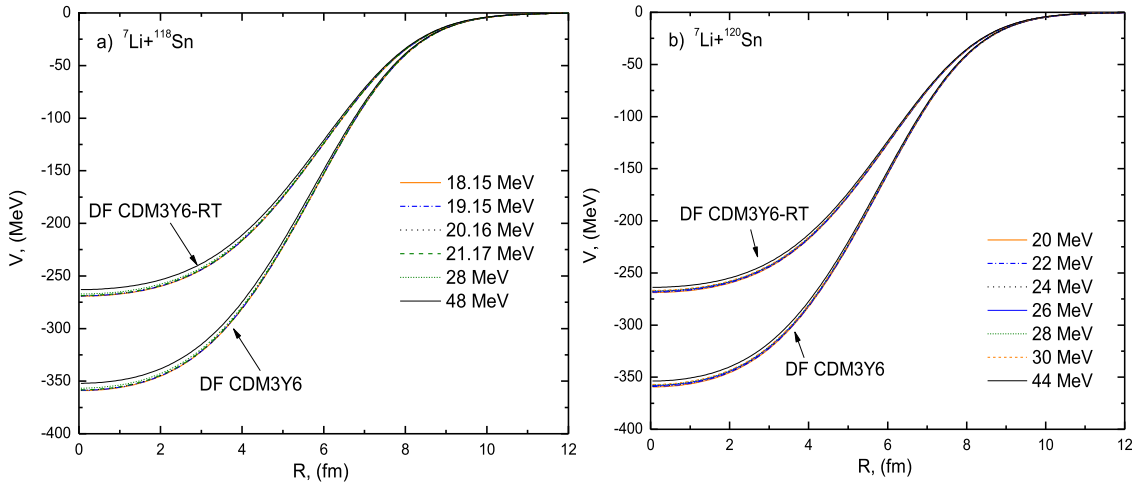

Fig. 2. (color online) DFP prepared using both CDM3Y6 and CDM3Y6-RT interactions for a) ^{7}Li+^{118}Sn at energies $E_{\rm lab}$ = 18.15, 19.15, 20.16, 21.17, 28, and 48 MeV and b) ^{7}Li+^{120}Sn at energies $E_{\rm lab}$ = 20, 22, 24, 26, 28, 30, and 44 MeV.

wave function generated from a WS potential with a radius of $0.667\times\left(4^{1/3}+3^{1/3}\right)$ fm, diffuseness of 0.65 fm, and depth tuned to achieve the cluster binding energy. In this analysis, it was critical to select the appropriate constituent potentials. The ^{7}Li + ^{118}Sn analysis incorporated t + ^{118}Sn potentials at 20 MeV [29] and α + ^{118}Sn potentials at 27 MeV [30]. Similarly, the ^{7}Li + ^{120}Sn analysis incorporated t + ^{120}Sn potentials at 20 MeV [29] and α + ^{120}Sn potentials at 26.1 MeV [31], all carefully validated against existing experimental data. The complete set of derived CFPs is presented in Fig. 3.

This multi-faceted theoretical framework enables a comprehensive investigation of the elastic scattering dynamics, systematically addressing the physical mechanisms influencing the interaction through increasingly sophisticated treatments of nuclear structure and reaction mechanisms. Each methodological approach provides complementary constraints on the potential forms and their parameters, collectively yielding a robust understanding of ^{7}Li scattering processes.

III. RESULTS AND DISCUSSION

A. Analysis of ^{7}Li + ^{118,120}Sn data using SPP

The elastic scattering ADs for the ^{7}Li + ^{118}Sn system at $E_{\rm lab}$ = 18.15–48 MeV [4–6] and for the ^{7}Li + ^{120}Sn system at $E_{\rm lab}$ = 20–44 MeV [7–9] were analyzed using the SPP, which provides a microscopic description of the nuclear interaction. Building upon the SPP2 formulation [32], we applied this approach to achieve a comprehensive description that incorporates the internal structure of the colliding nuclei. The real component of the potential was generated using the **REGINA** code framework, while the imaginary part was constructed as a scaled version of the real potential, maintaining a consistent radial dependence. The employed potential is given by

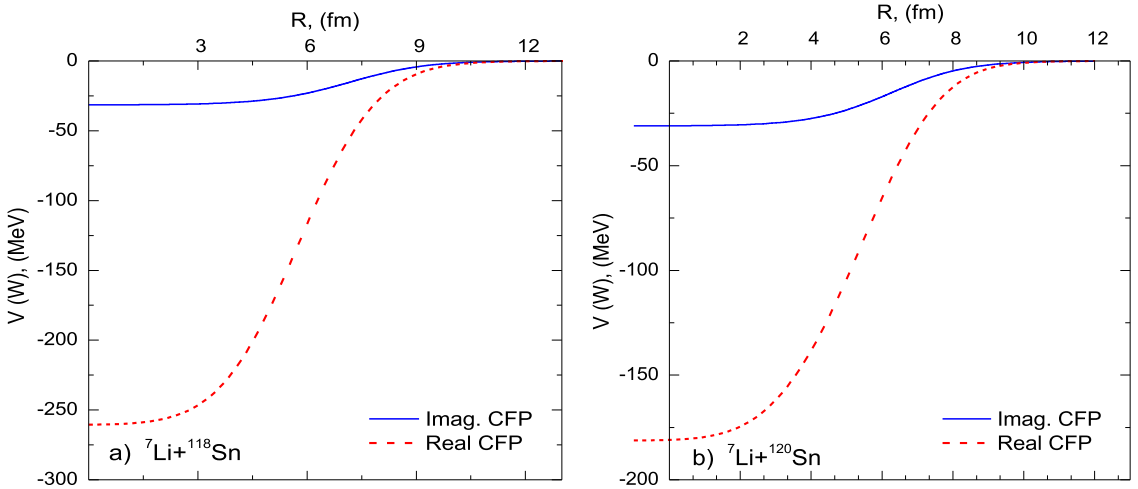

Fig. 3. (color online) Real and imaginary CFPs: a) ^{7}Li + ^{118}Sn system and b) ^{7}Li + ^{120}Sn system.

$$U(R) = V_C(R) - N_{RSPP}\, V^{DF}(R) - \mathrm{i}N_{ISPP}\, V^{DF}(R). \quad (8)$$

This formulation incorporates normalization factors for both real (N_{RSPP}) and imaginary (N_{ISPP}) components. The optimized values of these factors provide important physical insights into the interaction dynamics. As detailed in Table 1, the analysis consistently requires significant reduction of the real potential strength, with average normalization factors of 0.54±0.28 for ^{118}Sn and 0.60±0.05 for ^{120}Sn. This substantial reduction —corresponding to approximately 46% and 40% weakening of the bare potential strength—directly reflects the impact of ^{7}Li breakup on the elastic scattering channel. The energy dependence of these normalization factors is particularly pronounced near the Coulomb barrier region ($V_B \approx 21$ MeV), where coupling to breakup channels is most significant.

Table 1. Optimal potential parameters for the ^{7}Li + ^{118,120}Sn nuclear system using SPP. The values of (J_V), (J_W), and (σ_R) are displayed. The underlined parameters are fixed.

E /MeV	N_{RSPP}	N_{ISPP}	χ^2/N	σ_R /mb	J_V /MeV·fm^3	J_W /MeV·fm^3
			^{7}Li + ^{118}Sn			
18.15	0.931	0.1	0.1	8.74	382.64	41.1
	0.54	0.161	0.11	9.46	221.94	66.17
19.15	0.32	0.81	0.15	88.49	131.52	332.91
	0.54	0.670	0.16	81.06	221.94	275.37
20.16	0.357	0.746	0.24	161.7	146.73	306.61
	0.54	0.568	0.27	145.1	221.94	233.45
21.17	0.234	0.99	0.73	304.2	96.17	406.89
	0.54	0.60	1.0	259.5	221.94	246.6
28	0.677	0.476	100.6	1037	278.25	195.64
	0.54	0.363	118.2	958.6	221.94	149.19
48	0.734	0.624	2.5	2089	301.67	256.46
	0.54	0.389	7.86	1927	221.94	159.88
			^{7}Li + ^{120}Sn			
20	0.602	0.426	1.8	122.8	251.46	177.94
	0.6	0.427	1.9	122.9	250.2	178.36
22	0.632	0.414	4.1	355.3	263.99	172.93
	0.6	0.477	6.51	366.2	250.2	199.24
24	0.617	0.56	29.2	653.1	257.72	233.91
	0.6	0.57	30.3	652.0	250.2	238.09
26	0.502	0.43	21.3	810.9	209.69	179.61
	0.6	0.62	50.8	896.6	250.2	258.97
28	0.631	0.565	68.6	1083	263.57	236.00
	0.6	0.554	81.2	1072	250.2	231.41
30	0.631	0.439	100.1	1204	263.57	183.37
	0.6	0.433	113.3	1193	250.2	180.86
44	0.563	0.464	0.04	1892	229.99	189.54
	0.6	0.505	0.06	1892	250.2	210.94

As shown in Figs. 4 and 5, this approach successfully reproduces the experimental ADs across the entire energy range. For clarity, the presented ADs are displaced by a factor of 0.5. The optimal potential parameters extracted from these fits are presented in Table 1, along with σ_R and the corresponding volume integrals (J_V, J_W). The systematic behavior of these parameters provides important insights into the energy dependence of the ^{7}Li-nucleus interaction.

Additionally, we reproduced the ^{7}Li + ^{118,120}Sn ADs using only one adjustable parameter (N_{ISPP}), fixing N_{RSPP}

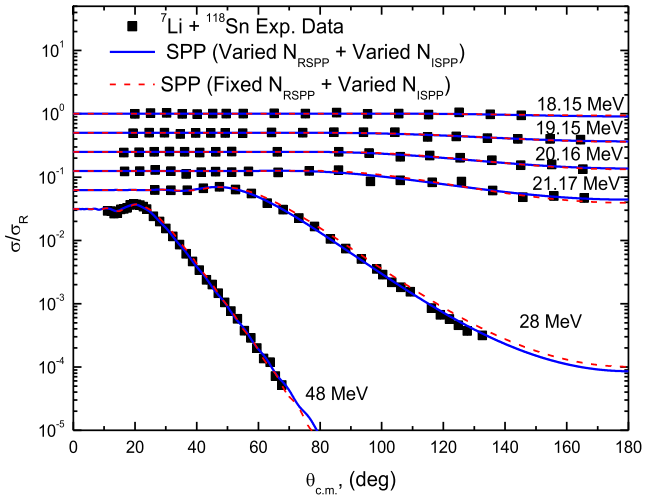

Fig. 4. (color online) Experimental ^{118}Sn (^{7}Li,^{7}Li)^{118}Sn ADs (squares) versus SPP calculations (curves) at E_{lab}= 18.15, 19.15, 20.16, 21.17, 28 and 48 MeV.

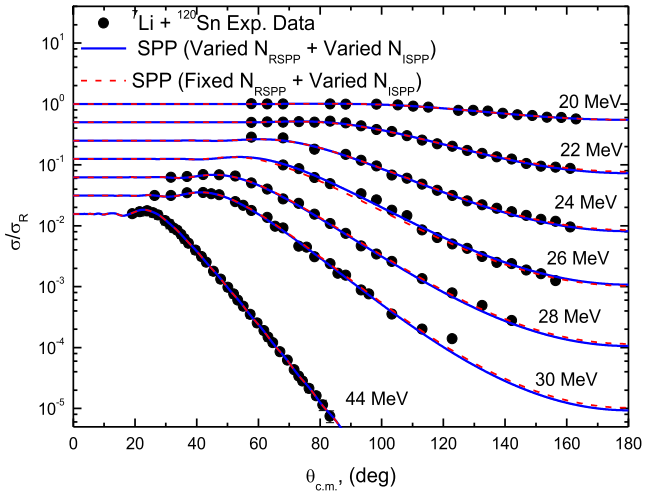

Fig. 5. (color online) Experimental ^{120}Sn(^{7}Li,^{7}Li)^{120}Sn ADs (circles) versus SPP calculations (curves) at E_{lab}= 20, 22, 24, 26, 28, 30 and 44 MeV.

at the aforementioned average normalization factors of (0.54 for ^{118}Sn) and (0.60 for ^{120}Sn). These results, presented as dashed curves in Figs. 4 and 5, agree well with the data. The optimal extracted N_{ISPP} values are listed in Table 1. The volume integrals derived from the SPP analyses using both the (varied N_{RSPP} + varied N_{ISPP}) and (fixed N_{RSPP} + varied N_{ISPP}) approaches exhibit behavior that is consistent with the breakup threshold anomaly (BTA) [33, 34]. This phenomenon, observed in scattering involving WB nuclei, is characterized by a decrease in the real potential strength (revealing a repulsive polarization potential) and an increase in the imaginary strength (enhanced absorption) as the energy approaches the Coulomb barrier. This contrasts with the normal threshold anomaly [35] observed with tightly bound nuclei. This systematic behavior emerges naturally from the microscopic foundation of the SPP. The success of this analysis highlights the manner in which the SPP framework incorporates the essential physics of WB projectile scattering, while maintaining a fundamental connection to microscopic nuclear structure. The required potential normalizations quantitatively capture the dynamic polarization effects from coupling to the breakup channel.

B. Analysis of ^{7}Li + ^{118,120}Sn data using CDM3Y6 interaction with and without RT

We further investigated the ^{7}Li + ^{118,120}Sn systems using the microscopic DF model with CDM3Y6 interactions, with and without the rearrangement term (RT). The comparison between the standard CDM3Y6 and CDM3Y6-RT results offers valuable insights into the importance of rearrangement effects in these scattering systems. The systematic differences between these approaches help quantify the mechanism by which such microscopic corrections influence the overall potential strength and energy dependence required to reproduce the experimental ADs. The employed central is

$$U(R) = V_C(R) - N_{RDF}\, V^{DF}(R) - \mathrm{i}N_{IDF}\, V^{DF}(R). \qquad (9)$$

The analysis introduces two adjustable parameters: N_{RDF} and N_{IDF} as normalization for the real and imaginary potential components, respectively. The imaginary component of the potential is generated by scaling the real folded potential. The DFP calculations using the CDM3Y6 interaction successfully reproduce the experimental ADs for the ^{7}Li + ^{118,120}Sn system, as evidenced by the good agreement depicted in Figs. 6 and 7. The best fit N_{RDF} and N_{IDF} parameters derived from the analyses (Table 2) provide key insights into the underlying interaction dynamics. For the ^{7}Li + ^{118}Sn system, the real DF potential strength requires substantial reduction with an average N_{RDF} value of 0.35 ± 0.19, corresponding to approximately 65% weakening of the bare potential. The ^{7}Li + ^{120}Sn system

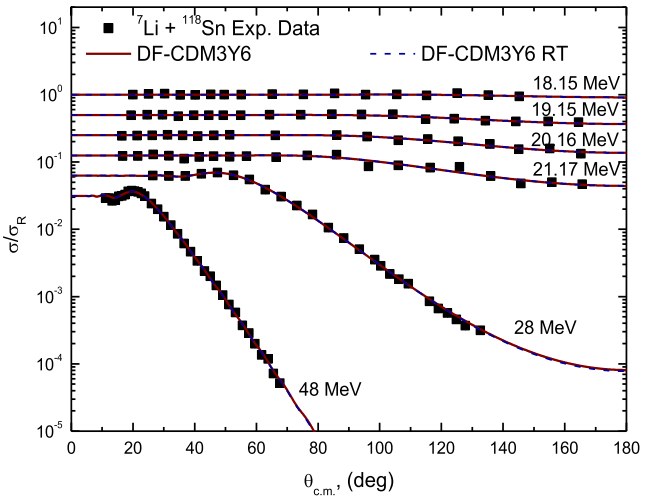

Fig. 6. (color online) Experimental between ^{118}Sn(^{7}Li,^{7}Li)^{118}Sn ADs (squares) versus DF calculations utilizing both CDM3Y6 (curves) and CDM3Y6-RT interactions (dashed curves) at E_{lab}= 18.15, 19.15, 20.16, 21.17, 28 and 48 MeV.

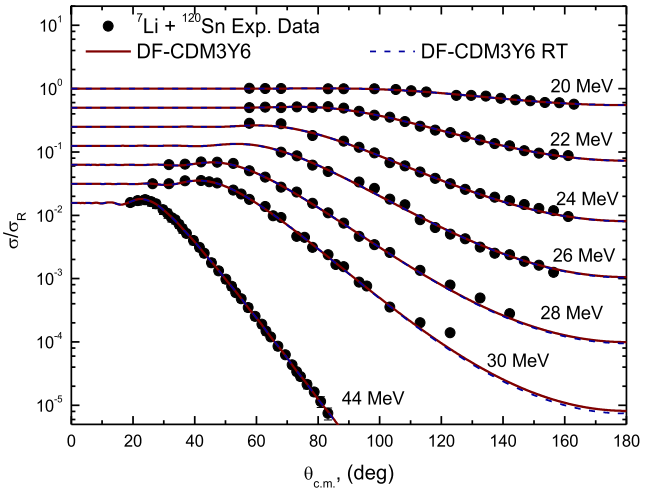

Fig. 7. (color online) Experimental ^{120}Sn(^{7}Li,^{7}Li)^{120}Sn ADs (circles) versus DF calculations utilizing both CDM3Y6 (curves) and CDM3Y6-RT interactions (dashed curves) at E_{lab}= 20, 22, 24, 26, 28, 30 and 44 MeV.

shows a similar, but somewhat less pronounced effect, with an average N_{RDF} of 0.41 ± 0.03. The inclusion of the rearrangement term through the CDM3Y6-RT modification yields comparable quality fits (Figs. 6 and 7), with only marginal differences in the required normalization. The ^{7}Li + ^{118}Sn system now shows an average N_{RDF} of 0.37 ± 0.20 (63% reduction), while the ^{7}Li + ^{120}Sn system yields 0.422 ± 0.03 (58% reduction). The minimal variation between the standard CDM3Y6 and CDM3Y6-RT results suggests that rearrangement effects play a secondary role compared to the dominant breakup dynamics in these systems.

Table 2. Optimized parameters for the ^{7}Li + ^{118,120}Sn systems using DF-CDM3Y6 interactions with/without RT, showing the fitted N_{RDF} and N_{IDF} values with corresponding J_V, J_W, and σ_R results.

E /MeV	Interaction model	N_{RDF}	N_{IDF}	χ^2/N	σ_R/mb	J_V/MeV·fm^3	J_W /MeV·fm^3
			^{7}Li + ^{118}Sn				
18.15	CDM3Y6	0.585	0.1	0.1	10.46	256.90	43.92
	CDM3Y6-RT	0.623	0.215	0.1	10.19	221.10	76.30
19.15	CDM3Y6	0.221	0.549	0.15	88.49	96.964	240.87
	CDM3Y6-RT	0.228	0.568	0.15	88.57	80.83	201.37
20.16	CDM3Y6	0.244	0.51	0.24	161.9	106.97	223.58
	CDM3Y6-RT	0.252	0.531	0.24	162.1	89.25	188.07
21.17	CDM3Y6	0.1	0.765	0.71	320.1	43.75	334.69
	CDM3Y6-RT	0.1	0.797	0.71	320.3	35.38	281.98
28	CDM3Y6	0.458	0.353	89.4	1044	199.44	153.71
	CDM3Y6-RT	0.477	0.386	84.3	1048	167.71	135.72
48	CDM3Y6	0.498	0.48	2.3	2115	213.20	205.49
	CDM3Y6-RT	0.524	0.536	2.3	2128	181.01	185.15
			^{7}Li + ^{120}Sn				
20	CDM3Y6	0.415	0.293	1.8	122.8	182.14	128.60
	CDM3Y6-RT	0.431	0.307	1.8	123.0	152.96	108.95
22	CDM3Y6	0.43	0.295	4.2	357.0	188.40	129.25
	CDM3Y6-RT	0.447	0.316	4.3	358.5	158.34	111.93
24	CDM3Y6	0.414	0.404	30.69	657.9	181.08	176.70
	CDM3Y6-RT	0.428	0.436	31.6	661.0	151.34	154.17
26	CDM3Y6	0.338	0.316	20.5	817.8	147.54	137.93
	CDM3Y6-RT	0.351	0.345	20.0	822.2	123.87	121.75
28	CDM3Y6	0.423	0.409	73.2	1089	184.38	178.27
	CDM3Y6-RT	0.439	0.442	76.4	1092	154.64	155.70
30	CDM3Y6	0.427	0.321	99.6	1210	185.41	139.38
	CDM3Y6-RT	0.447	0.349	99.8	1213	157.17	122.72
44	CDM3Y6	0.39	0.375	0.03	1931	167.66	161.21
	CDM3Y6-RT	0.414	0.431	0.03	1953	143.77	149.68

C. Analysis of ^{7}Li + ^{118,120}Sn data using CFP

The remarkable clusterization tendency of ^{7}Li, particularly its preferential dissociation into the $t + \alpha$ configuration at ~ 2.468 MeV, motivates our application of the CFP approach within the microscopic CFM framework. This method effectively reproduces the ^{7}Li + ^{118,120}Sn ADs by the following central potential formulation:

$$U(R) = V_C(R) - N_{RCF}\ V^{CF}(R) - \mathrm{i}\ N_{ICF}\ W^{CF}(R). \qquad (10)$$

The ^{7}Li + ^{118,120}Sn ADs were reproduced using two parameters: N_{RCF} (real CFP normalization) and N_{ICF} (imaginary CFP normalization). The CFP based calculations successfully reproduced the ^{7}Li + ^{118,120}Sn ADs across all measured energies and the angular range, as demonstrated in Figs. 8 and 9. Excellent agreement was achieved overall; however, the higher χ^2 values observed at 28 and 48 MeV for ^{118}Sn and at 28 and 30 MeV for ^{120}Sn originate from minor discrepancies at backward angles ($\theta > 110°$). These deviations likely arise from other reaction channels and are not accounted for in the double and cluster folding calculations. They become significant at these energies and angles.

The analysis within the CFP framework reveals $\boldsymbol{N_{RCF}}$ values of 0.50 ± 0.23 and 0.40 ± 0.09 for ^{7}Li + ^{118}Sn and ^{7}Li + ^{120}Sn systems, respectively (Table 3), corresponding to ~50% and 60% reductions in the real CFP strength. This consistent reduction requirement mirrors our observations in the SPP, DF-CDM3Y6, and DF-CDM3Y6-RT

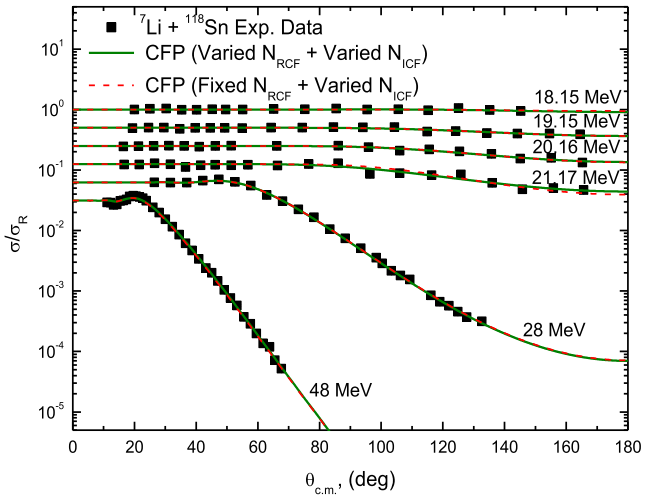

Fig. 8. (color online) Experimental ^{118}Sn(^{7}Li,^{7}Li)^{118}Sn ADs at E_{lab}= 18.15, 19.15, 20.16, 21.17, 28, and 48 MeV (squares) compared to the CFP calculations (curves).

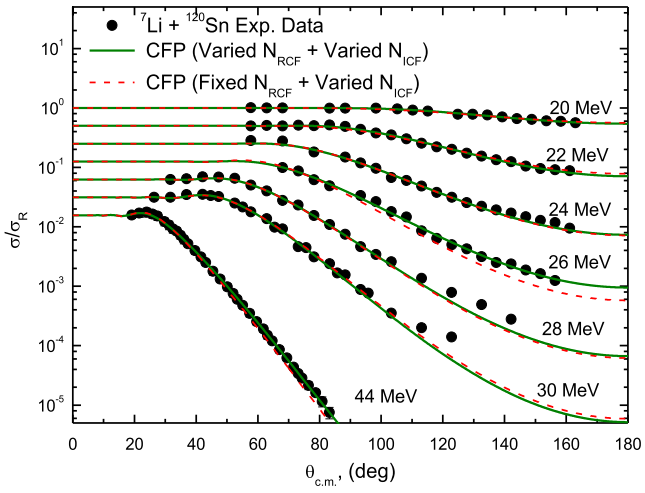

Fig. 9. (color online) Experimental ^{120}Sn(^{7}Li,^{7}Li)^{120}Sn ADs at E_{lab}= 20, 22, 24, 26, 28, 30, and 44 MeV (circles) compared to the CFP calculations (curves).

analyses, creating a coherent picture across different theoretical approaches. This consistency strongly suggests that the required normalization primarily reflects dynamic polarization effects arising from the weak binding and cluster nature of ^{7}Li, rather than being an artifact of any particular model [36−41]. The slightly greater reduction observed for ^{120}Sn compared to ^{118}Sn may indicate subtle mass-dependent variations in the modification of the effective potential by the breakup process; however, both systems clearly demonstrate the characteristic signatures of WB projectile scattering [36−40]. These results collectively highlight how the CFM provides both quantitative agreement with experimental data and valuable physical insight into the underlying reaction mechanisms. By treating the α and t components explicitly, the approach captures the essential features of the ^{7}Li-nucleus interaction that might be obscured by more phenomenological treatments.

Table 3. Optimized parameters for the ^{7}Li + ^{118,120}Sn systems obtained from calculations within the CFP. The values of σ_R, J_V, and J_W are provided. The underlined parameters are fixed.

E /MeV	N_{RCF}	N_{ICF}	χ^2/N	σ_R /mb	J_V /MeV·fm^3	J_W /MeV·fm^3
			^{7}Li + ^{118}Sn			
18.15	0.905	0.1	0.1	11.10	297.87	6.77
	0.5	0.108	0.11	9.81	164.58	7.31
19.15	0.502	0.581	0.17	93.62	165.23	39.33
	0.5	0.581	0.17	93.56	164.58	39.33
20.16	0.435	0.638	0.23	172.1	143.18	43.19
	0.5	0.580	0.23	163.8	164.58	39.27
21.17	0.192	0.99	0.7	338.3	63.19	67.02
	0.5	0.607	1.0	272.5	164.58	41.09
28	0.505	0.788	104.8	1107	166.22	53.35
	0.5	0.793	105.4	1108	164.58	53.69
48	0.455	1.355	3.6	2293	149.76	91.73
	0.5	1.49	4.6	2342	164.58	100.87
			^{7}Li + ^{120}Sn			
20	0.545	0.368	1.4	131.2	158.58	25.89
	0.4	0.510	3.4	153.8	116.38	35.88
22	0.475	0.492	5.6	385.1	138.22	34.61
	0.4	0.647	13.5	421.3	116.38	45.52
24	0.391	0.732	50.2	708.7	113.77	51.50
	0.4	0.708	50.4	702.5	116.38	49.81
26	0.294	0.696	17.16	896.6	85.548	48.96
	0.4	0.544	81.16	864.5	116.38	38.27
28	0.384	0.781	151.7	1150	111.74	54.94
	0.4	0.756	154.8	1144	116.38	53.18
30	0.428	0.627	130.1	1263	124.54	44.11
	0.4	0.671	140.2	1274	116.38	47.21
44	0.315	1.14	0.08	1892	91.66	80.20
	0.4	0.99	1.89	2115	116.38	69.65

Moreover, we reproduced the ^{7}Li + ^{118,120}Sn ADs using one adjustable parameter, N_{ICF}, fixing the N_{RCF} at the aforementioned average extracted normalizations (0.50 for ^{118}Sn) and (0.40 for ^{120}Sn). These results, presented as dashed curves in Figs. 8 and 9, agree well with the AD data. The optimal extracted N_{ICF} values from both (varied N_{RCF} + varied N_{ICF}) and (fixed N_{RCF} + varied N_{ICF}) approaches are listed in Table 3. The extracted J_W values show a non-vanishing nature below the barrier, a signature of the BTA phenomenon.

D. Analysis of ^{7}Li + ^{118,120}Sn data using CDCC method

Our systematic analysis using various potential models (DF-CDM3Y6, DF-CDM3Y6-RT, SPP, and CFP) consistently demonstrates the need to reduce the real potential strength by approximately 65%, 63%, 46%, and 50% for the ^{7}Li + ^{118}Sn system, and by 60%, 58%, 41%, and 60% for ^{7}Li + ^{120}Sn. This systematic reduction requirement originates from the significant breakup effects of ^{7}Li in the nuclear field of the Sn targets. Such effects are explicitly and accurately accounted for within the CDCC framework implemented through **FRESCO** calculations.

The core concept of the CDCC method is truncating and discretizing the continuum above the ^{7}Li breakup threshold into a series of momentum bins, each treated as an excited state. This methodology allows the coupling effects of these discretized continuum states to be incorporated into the reaction calculations. This approach generates a repulsive real dynamical polarization potential (DPP) [42, 43] through continuum couplings, which explains the observed strength reduction. The extent of the model space, defined by the maximum momentum (k_{max}), was adjusted based on the bombarding energy. For bombarding energies between 18.15 and 20 MeV, the momentum space (k) above the ^{7}Li breakup threshold was truncated at k_{max} = 1.25 fm^{-1} (corresponding to E_{max} = 19.05 MeV). For energies greater than 20 MeV and up to 30 MeV, k_{max} was set to 1.5 fm^{-1} (E_{max} = 27.44 MeV). For the two highest energies studied, the model space was extended to k_{max} = 2 fm^{-1} (E_{max} = 37.34 MeV).

A critical aspect of CDCC calculations is ensuring their convergence, i.e., the results must be independent of the choice of numerical parameters (*e.g.*, matching radius, R_{match}, and integration step-size, *hcm*) or model space parameters (*e.g.*, momentum-bin width, Δk, maximum momentum, k_{max}, and the inclusion of pseudo-states with different angular momenta, L). A series of test calculations were performed for the case of ^{7}Li+^{120}Sn at 28 MeV. These tests confirmed that the calculations converged with the numerical parameters (R_{match} = 40 fm, *hcm* = 0.04 fm), as shown in Fig. 10 (a) and Fig. 10 (b). The convergence with respect to the model space was also examined. As shown in Fig. 10 (c), the calculations converged with a bin width of Δk = 0.25 fm^{-1}. The results for Δk = 0.2 and 0.25 fm^{-1} are very similar, which is consistent with the previous study of Sakuragi *et al.* [42]. Furthermore, the convergence test against the maximum momentum value confirms that the calculations converge

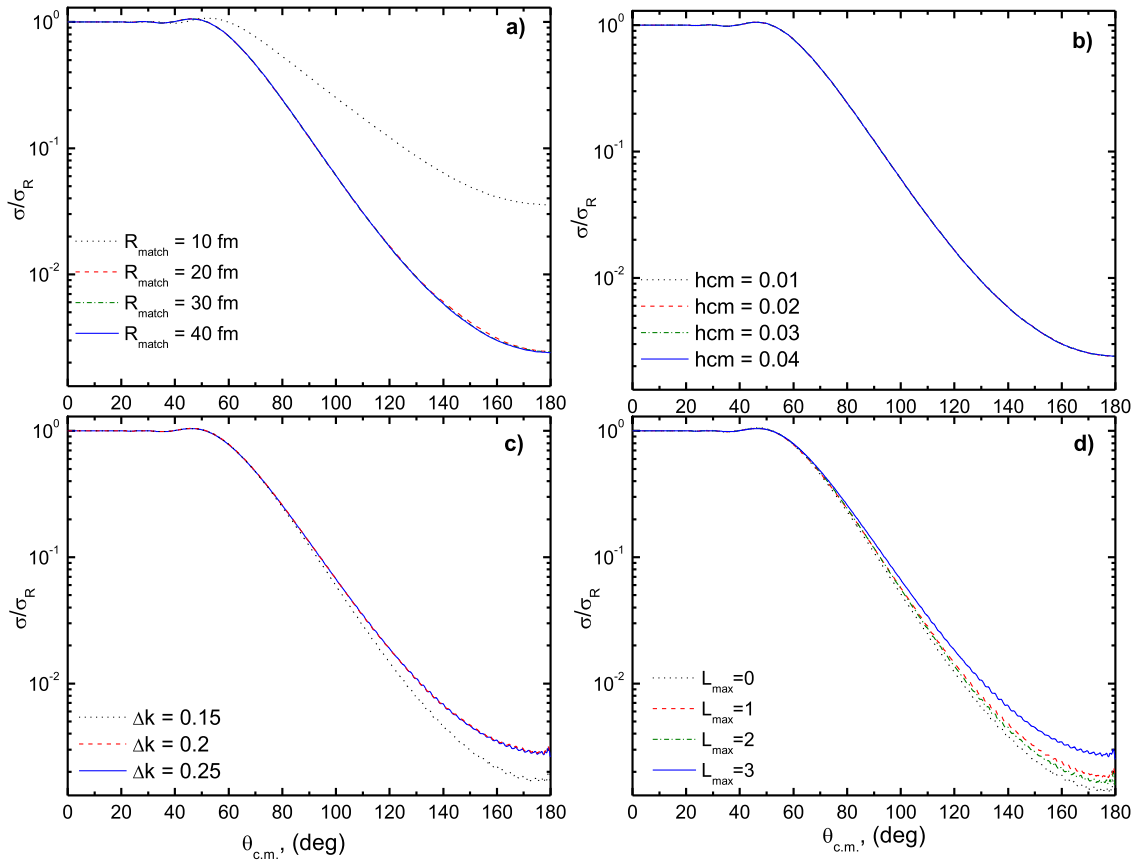

Fig. 10. (color online) Convergence tests of the CDCC calculations for ^{7}Li + ^{120}Sn at 28 MeV with respect to a) R_{match}, b) *hcm*, c) Δk, and d) L_{max}.

with k_{max} = 0.75 fm^{-1}, as the momentum bins above this value do not contribute significantly. Finally, the model was tested with respect to the included partial waves. Figure 10 (d) shows the pseudo-states with L= 0, 1, 2, 3, 4. The calculations show convergence at L =3.

Guided by these convergence tests, the final CDCC treatment incorporated continuum states by momentum bin discretization ($0.0 \le k \le 0.75$ fm^{-1} with Δk = 0.25 fm^{-1}) [44] above the 2.468 MeV breakup threshold. This included the significant resonant states (7/2$^-$, E_x= 4.652 MeV and 5/2$^-$, E_x = 6.604 MeV) with L=3 and the bound non-resonant state (1/2$^-$, E_x= 0.4776 MeV) in addition to the ^{7}Li ground state (3/2$^-$, E_x= 0.0 MeV). For the coupling and diagonal potentials, we employed the cluster folding procedure outlined in Eqs. (6) and (7) using the same t + ^{118}Sn (^{120}Sn) and α + ^{118}Sn (^{120}Sn) potentials as in our CFM calculations. For the CDCC method, the projectile's wave functions must be calculated first. The ^{7}Li ground state and the 1/2$^-$ bound state were modeled as a $2P_{3/2}$ configuration using a WS potential with a radius of $0.667 \times \left(4^{1/3} + 3^{1/3}\right)$ fm, diffuseness of 0.65 fm, and depth tuned to achieve the cluster binding energy (V_0 = 96.25 MeV). The two resonant states (7/2$^-$ and 5/2$^-$) were modeled as $1D_{7/2}$ and $1D_{5/2}$ configurations using a WS potential with the same geometry and depths of 96.8894 and 88.8348 MeV, respectively. This two-body cluster approach for ^{7}Li is further supported by similar findings for the ^{6}Li nucleus. Despite ^{6}Li having a dominant d+α cluster structure, a full four-body (n+p+α) CDCC analysis of ^{6}Li + ^{209}Bi scattering revealed that the dominant breakup effect was still well-captured by the simpler d+α two-body breakup channels [45]. Considering the dominant role of L=3 resonances [36, 44, 46, 47], our CDCC model included one non-resonant (1/2$^-$) and two resonant states (7/2$^-$ and 5/2$^-$), with widths of 0.2 and 2.0 MeV, respectively.

As shown in Figs. 11 and 12, the CDCC calculations achieve good agreement with experimental ADs without requiring potential normalization. The remaining minor deviations likely reflect limitations in the model space truncation and discretization or small uncertainties in the input cluster potentials. A slight oscillation observed in the calculations at backward angles for the ^{120}Sn system (Fig. 12) is a genuine result arising from the specific interference pattern between the elastic and breakup channels at these large angles. Importantly, the success of these parameter-free calculations validates our earlier findings from simpler models, confirming that the substantial potential reductions indeed originate from dynamic polarization effects due to continuum coupling. The CDCC results provide particularly clear evidence that the DPP generated by breakup channel coupling accounts for the reduced effective potential strength needed in the other approaches. This physical interpretation unifies our understanding across all theoretical methods em-

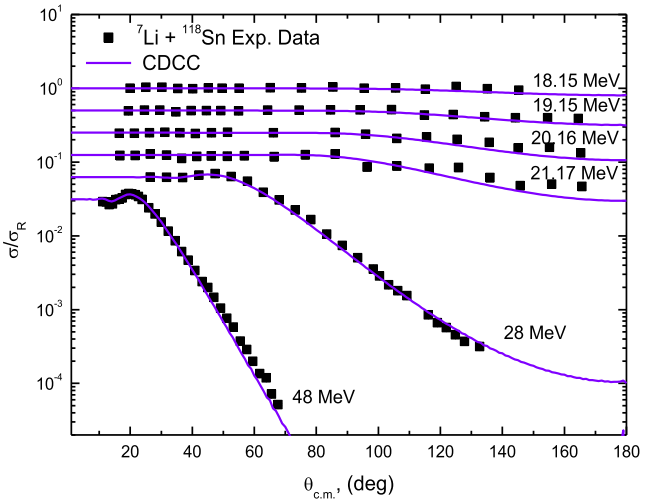

Fig. 11. (color online) Experimental ^{118}Sn(^{7}Li,^{7}Li)^{118}Sn ADs (circles) versus CDCC calculations (curves) E_{lab}= 18.15, 19.15, 20.16, 21.17, 28 and 48 MeV.

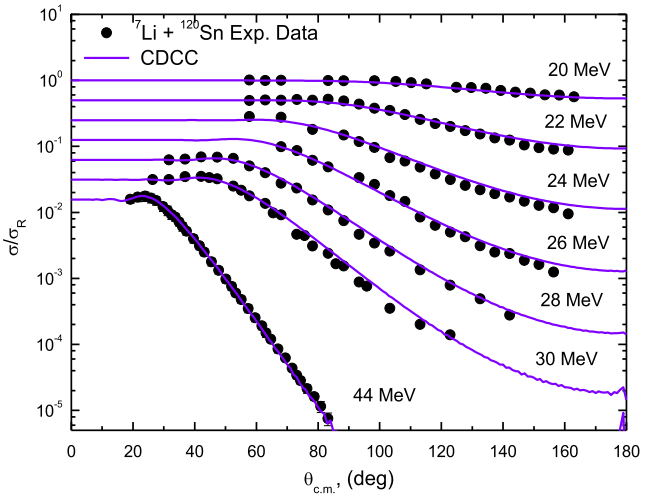

Fig. 12. (color online) Experimental ^{120}Sn(^{7}Li,^{7}Li)^{120}Sn ADs (circles) versus CDCC calculations (curves) at E_{lab}= 20, 22, 24, 26, 28, 30, and 44 MeV.

ployed in this comprehensive study of ^{7}Li scattering.

Figure 13 displays the energy-dependent reaction cross sections for the ^{7}Li + ^{118,120}Sn systems, calculated using multiple theoretical approaches (SPP, CDM3Y6, CDM3Y6-RT, CFM, and CDCC). The calculated cross sections exhibit systematic energy dependence that can be parameterized by the following second-order polynomial fits:

$$\sigma_R(E) = -2905.6 + 190.5\,E - 1.78\,E^2, \quad (11)$$

$$\sigma_R(E) = -3747.5 + 246.9\,E - 2.76\,E^2. \quad (12)$$

The quadratic energy dependence revealed by these polynomial fits reflects characteristic nuclear reaction dy-

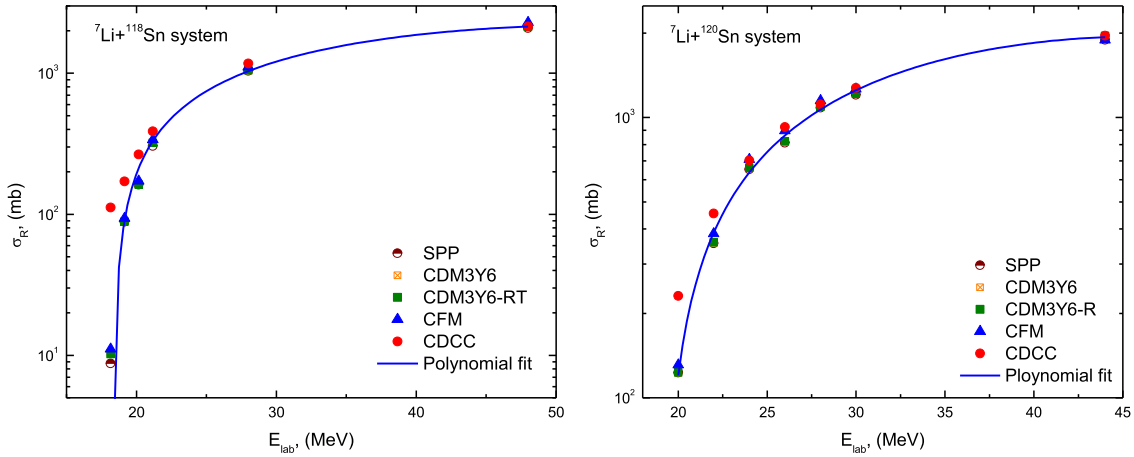

Fig. 13. (color online) Energy versus the extracted σ_R values for ^{7}Li + ^{118,120}Sn systems using the different employed approaches: SPP, CDM3Y6, CDM3Y6-RT, CFM, and CDCC.

namics observed in heavy-ion systems. For both Sn isotopes, the reaction cross sections initially increase with energy owing to greater penetration of the Coulomb barrier, then gradually saturate at higher energies as nuclear interaction probabilities decrease. The systematically larger coefficients observed for the ^{120}Sn system compared to ^{118}Sn quantitatively capture the expected enhancement in nuclear absorption for the heavier isotope, consistent with established mass-dependent trends in heavy-ion reactions. The negative quadratic terms in both expressions physically represent the transition between competing mechanisms. At lower energies, cross sections are dominated by barrier penetration effects, while at higher energies, the reduced interaction time and increased importance of direct reaction channels become predominant.

This energy dependence pattern appears consistently across all theoretical approaches shown in Fig. 13, nevertheless the model-dependent variations particularly highlight the significance of properly accounting for breakup effects when dealing with WB projectiles such as ^{7}Li. The polynomial parameterizations provide a useful quantitative framework for comparing the energy evolution of reaction probabilities across different theoretical treatments. Although the extracted σ_R values from the various employed approaches are generally in close agreement, those obtained from the CDCC results show a significant enhancement at the lowest studied energies.

IV. SUMMARY

This systematic study of ^{7}Li elastic scattering from ^{118,120}Sn nuclei across an energy range of 18–48 MeV reveals the dominance of the projectile's weak binding and cluster structure in governing the reaction dynamics. All employed theoretical approaches from folding models to microscopic CDCC calculations consistently demonstrate that accurate descriptions require 40−65% reductions in the real potential strength. This substantial renormalization directly reflects the dynamic polarization potential arising from coupling to breakup channels.

While simpler models achieve good fits through empirical normalization factors, the CDCC framework successfully reproduces the data without adjustments by explicitly treating continuum states, confirming these reductions as physical effects rather than artifacts. The cluster folding model's success further underscores the importance of properly accounting for the α+t structure of^{7}Li .

The reaction cross sections exhibit characteristic energy dependence, initially rising owing to barrier penetration and saturating at higher energies. Polynomial fits capture these trends, while revealing subtle mass-dependent differences between targets. Notably, the conventional threshold anomaly is absent, replaced by smooth energy dependence consistent with persistent breakup effects across the studied range.

Collectively, these results establish that reliable descriptions of WB nuclear systems must incorporate both cluster degrees of freedom and continuum coupling. This provides a unified understanding that bridges phenomenological and microscopic approaches, offering valuable benchmarks for future theoretical developments. The CDCC method emerges as a particularly robust approach for such systems, though appropriately normalized folding potentials offer a practical and effective alternative when full coupled-channel calculations are impractical.

References

[1] P. R. S. Gomes *et al.*, Few Body Syst. **57**, 165 (2016)
[2] L. F. Canto, P. R. S. Gomes, R. Donangelo *et al.*, Phys. Rep. **424**, 1 (2006)
[3] L. Fimiani *et al.*, Phys. Rev. C **86**, 044607 (2012)

[4] K. O. Pfeiffer, E. Speth, and K. Bethge, Nucl. Phys. A **206**, 545 (1973)
[5] A. Kundu *et al*., Phys. Rev. C **99**, 034609 (2019)
[6] A. F. Zeller *et al*., Nucl. Phys. A **309**, 255 (1978)
[7] V. A. B. Zagatto *et al*., Phys. Rev. C **95**, 064614 (2017)
[8] A. Kundu *et al*., Phys. Rev. C **95**, 034615 (2017)
[9] G. Tungate *et al*., J. Phys. G: Nucl. Phys. **12**, 1001 (1986)
[10] K. Zerva *et al*., Eur. Phys. J. A **48**, 102 (2012)
[11] V. A. B. Zagatto *et al*., J. Phys. G: Nucl. Phys. **43**, 055103 (2016)
[12] M. A. G. Alvarez *et al*., Phys. Rev. C **100**, 064602 (2019)
[13] Y. Hirabayashi, Y. Sakuragi, and M. Tanifuji, Phys. Lett. B **318**, 32 (1993)
[14] Y. Sakuragi, M. Yahiro, M. Kamimura *et al*., Nucl. Phys. A **462**, 173 (1987)
[15] V. V. Sargsyan *et al*., Phys. Rev. C **90**, 064601 (2014)
[16] J. Cook, Nucl. Phys. A **388**, 153 (1982)
[17] Yongli Xu *et al*., Phys. Rev. C **97**, 014615 (2018)
[18] Y. P. Xu and D. Y. Pang, Phys. Rev. C **87**, 044605 (2013)
[19] Wen-Di Chen *et al*., Chin. Phys. C **44**, 054109 (2020)
[20] A. K. Basak *et al*., EPL **94**, 62002 (2011)
[21] E. Bauge, J. P. Delaroche, and M. Girod, Phys. Rev. C **58**, 1118 (1998)
[22] E. Bauge, J. P. Delaroche, and M. Girod, Phys. Rev. C **63**, 024607 (2001)
[23] I. J. Thompson, Comput. Phys. Rep. **7**, 167 (1988)
[24] B. V. Carlson, D. Hirata, Phys. Rev. C **62**, 054310 (2000)
[25] I. I. Gontchar, M. V. Chushnyakova, Comput. Phys. Commun. **181**, 168 (2010)
[26] D. T. Khoa *et al*., Phys. Rev. C **56**, 954 (1997)
[27] D. T. Khoa and W. Von Oertzen, Phys. Lett. B **304**, 8 (1993)
[28] D. T. Khoa, N. H. Phuc, D. T. Loan *et al*., Phys. Rev. C **94**, 034612 (2016)
[29] E. R. Flynn *et al*., Phys. Rev. **182**, 1113 (1969)
[30] A. Palumbo *et al*., Phys. Rev. C **85**, 035808 (2012)
[31] P. Mohr *et al*., Phys. Rev. C **82**, 044606 (2010)
[32] L. C. Chamon, B. V. Carlson, and L. R. Gasques, Comp. Phys. Comm. **267**, 108061 (2021)
[33] M. S. Hussein, P. R. S. Gomes, J. Lubian *et al*., Phys. Rev. C **73**, 044610 (2006)
[34] P. R. S. Gomes *et al*., Phys. Rev. C **70**, 054605 (2004)
[35] G. R. Satchler , Phys. Rep. **199**, 147 (1991)
[36] Sh. Hamada and A. A. Ibraheem, Int. J. Mod. Phys. E **31**, 2250019 (2022)
[37] A. Morzabayev *et al*., Chin. Phys. C **48**, 024103 (2024)
[38] Norah A. M. Alsaif *et al*., Revista Mexicana de Fisica **69**, 021201 (2023)
[39] Sh. Hamada *et al*., Pramana J. Phys **97**, 39 (2023)
[40] Sh. Hamada and Awad A. Ibraheem, Nucl. Phys. A **1030**, 122590 (2023)
[41] Sh. Hamada *et al*., Int. J. Mod. Phys. E **32**, 2350015 (2023)
[42] Y. Sakuragi, M. Yahiro, and M. Kamimura, Prog. Theor. Phys. **89**, 136 (1986)
[43] C. Mahaux, H. Ngo, and G. R. Satchler, Nucl. Phys. A **449**, 354 (1986)
[44] K. Rusek, J. Gomez-Camacho, I. Martel-Bravo *et al*., Nucl. Phys. A **614**, 112 (1997)
[45] S. Watanabe, T. Matsumoto, K. Ogata *et al*., Phys. Rev. C **92**, 044611 (2015)
[46] N. Keeley and K. Rusek, Phys. Lett. B **427**, 1 (1998)
[47] N. Keeley, K. W. Kemper, O. Momotyuk *et al*., Phys. Rev. C **77**, 057601 (2008)